Advanced Steel Construction – Vol. 19 No. 3 (2023) 293–307
DOI:10.18057/IJASC.2023.19.3.9

EXPERIMENTAL STUDY ON MECHANICAL PERFORMANCE OF BUCKLING-RESTRAINED BRACE ON FRAMES WITH HIGH-STRENGTH CONCRETE-FILLED SQUARE STEEL TUBE COLUMNS

Chuan-Zheng Ma *, Guo-Chang Li and Zhe-Yuan Wang

Department of Civil Engineering, Shenyang Jianzhu University, Shenyang 110168
** (Corresponding author: E-mail: 502699131@qq.com)*

ABSTRACT

Using buckling-restrained braces (BRBs) in frames with high-strength concrete-filled square steel tube columns(HSCFSSTC) can solve issues such as brittle failure and low lateral stiffness. To investigate the mechanical performance of buckling-restrained brace frames(BRBFs), an experiment study was conducted. The investigation involved the design and analysis of a frame system composed of BRBs, HSCFSSTC and H-shaped steel beams. Sub-structures at a 1/3 scale with two types of connections, welded and pin connections, were subjected to pseudo-static tests. The influence of BRBF connection types on the plastic hinge formation mechanism, load-bearing capacity, energy dissipation capacity and stress magnitude of the connection gusset plates was examined. After the test, ABAQUS software was used for finite element analysis of the specimen, and the simulation results were in good agreement with the experimental results.Based on the results, both the welded and pin-connected specimens formed plastic hinges at column bases and the beam ends, which ensured the energy dissipation performance of BRBs. Pin connections were found to exhibit noticeable slippage during loading due to the presence of holes. However, the study found that the plastic hinge formation mechanism, load-bearing capacity, and lateral stiffness of the frames with the two connection types were similar. Furthermore, there was no significant difference in the load-bearing capacity, stress distribution, and magnitude between the two connection types. Nevertheless, welded connections demonstrated a greater potential for broader application as they allowed the BRB to resist horizontal seismic forces earlier than pin connections.

ARTICLE HISTORY

Received: 25 April 2023
Revised: 30 May 2023
Accepted: 20 June 2023

KEYWORDS

Buckling-restrained brace;
High-strength concrete;
Pseudo-static test;
Welded connection;
Pin connection

1. Introduction

High-strength concrete-filled square steel tube columns are characterized by their small cross-sectional dimensions and lightweight, which have contributed to their widespread use in high-rise and super high-rise structures[1-4]. The reduction in column cross-section decreases the lateral stiffness of the structure, which can lead to increased story drift in the frame and make it difficult to meet seismic design requirements. Therefore, the use of BRB in frames can enhance the lateral stiffness of the system, dissipate seismic energy, as well as improve its overall seismic performance. [5-8]. The BRB in a frame with HSCFSSTC can mitigate the brittleness of high-strength concrete and fully utilize its performance, enhancing the safety and economy of the structure. With promising prospects for application and promotion, ensuring the connection reliability of BRBF connections is one of the key factors to consider.

Connections between BRBs and steel frames usually adopt three forms: bolted, welded and pin connections[9]. Bolted connections offer the advantages of simple construction methods but have drawbacks such as requiring more bolts and higher installation precision during construction, the transition segments （unrestrianed non-yielding segments） of BRB are longer, and the in-plane and out-of-plane bending stiffnesses are relatively smaller, making them prone to out-of-plane instability failure. For example, Keh-Chuuan Tsai et al. [10, 11] performed quasi-dynamic tests on a three-story concrete-filled tubular steel (CFST) structure with three full-size holes and bolted connections between the BRB and the structure. It was found that for a ply drift angle of 0.025 rad, the torsional deflection of the reinforcement leads to out-of-plane instability of the BRB. Similarly, Wang Jingfeng[12] and Li Beibei[13] conducted pseudo-static tests on five different types of connections used between BRBs and steel frames under cyclic loading conditions. In bolted connection specimens, out-of-plane deformation of the BRBF connection segment and reduced load-bearing capacity occurred when the story drift angle was around 1%. Mingming Jia et al. [14] performed the pseudo-static test on a two-story steel structure and a scaled-down passageway bolted between the BRB and the structure. When the drift angle is 0.026 rad, out-of-plane instability failure occurred in the BRBF connection portion, ending the experiment.

Pin connections offer advantages such as ease of construction and not transfering bending moments. However, when the connection shaft and gusset plate processing precision are insufficient, the BRB may not be able to bear horizontal shear forces at smaller story drift angles. Keith D. Palmer et al.[15] conducted pseudo-static tests on a 2-story single-bay spatial frame with pin connections between the BRB and the frame under bidirectional loading. The results showed that under bidirectional loading, the BRB could withstand large plastic deformations. However, due to the gap between the gusset plate and the pin shaft, the BRB core was not loaded during the transition between tension and compression, resulting in a horizontal slippage plateau on the axial force-displacement curve of the BRB. Junda E.[16] conducted cyclic tests on three diagonally braced frame sub-structures under cyclic loading and found that all three specimens with pin connections exhibited noticeable horizontal slippage plateau in the hysteresis curves. Similar slippage phenomena were observed in the experimental studies by Wang Jingfeng[12], Li Beibei[13], and others[17, 18].

Keh-Chyuan Tsai et al.[19] conducted a comparative analysis of welded connections and bolted connections in BRBFs. The results demonstrated that the transition segments of welded BRBs was shorter than that of bolted BRBs, which reduces their susceptibility to out-of-plane instability failure. The frames with welded connections had smaller story drift compared to the frames with bolted connections. Wang Cuihong[20] conducted static and dynamic elastoplastic analyses on three 8-story BRBFs, examining the behavior of beam-to-column connections that were either welded and bolted. The results indicated that both welded and bolted connections in the BRBF exhibited good ductility, leading to a global failure mechanism. The BRBF with welded connections at the first-story exhibited significantly higher load-bearing capacity and lateral stiffness compared to those with bolted connections. Sheng Pei et al.[21] performed pseudo-static tests on two single-story single bay BRBFs that had welded connections. The experimental results revealed that the BRBF with welded connections exhibited superior ductility and energy dissipation capability. Studies[19-21] on the welded BRBF connections have indicated that the structural performance of frames with welded connections was superior to those of bolted connections. However, few comparative analyses have been conducted on the structural performance of BRBFs with welded and pin connections. The limited understanding of the advantages and features of welded connections among designers is impeding the promotion and adoption of this connection type.

To investigate the structural performance of BRBFs with welded connections between BRBs and HSCFSSTC, this study designed two single-story single-bay planar frames with H-shaped steel beams. The BRBF adopted two connection methods: welded and pin connections. These two test frameworks were tested quasi-statically in the laboratory. After conducting the experiments, a comparative analysis of the structural performance of the two frames was carried out. In addition, the specimens were modeled using ABAQUS finite element software, facilitating a comparative analysis of the experimental results against the simulation results.

2. Experimental overview

2.1. Design of the prototype structure

In order to determine the parameters of the specimen, MIDAS was used for structural design. A 16-story 3×5 span space frame structure with BRB consisting of square steel columns filled with high-strength concrete and H-beams was designed. The total height of the structure is 58.2 meters, with the first floor at 4.2 meters and the second through sixteenth floors at 3.6 meters each. The columns in the structure were constructed using 450mm wide, 10 mm thick square steel tubes of Q460 steel and C100 concrete. The beam cross-section dimensions were H450×9×280×14 mm, and all steel beams used Q345 steel. The BRB core segment used Q235 steel. The structural plan layout is shown in Fig. 1, with a longitudinal span of 5×6=30 m and a transverse span of 3×6=18 m.

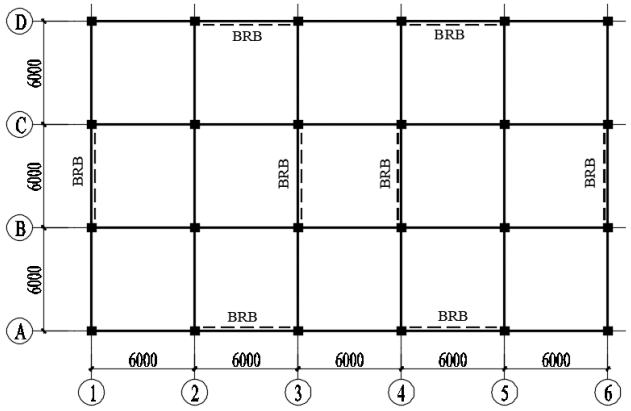

Fig. 1 Structural plan layout

The main design parameters of the prototype structure were as follows: a seismic fortification intensity of 7 degrees, earthquake grouping of groups 3, class 4 site, site characteristic period T_g=0.9s, and design basic seismic acceleration of 0.15g. The floor had a dead load of 4.5 kN/m^2 and a live load of 3 kN/m^2. The seismic performance of the frame met the relevant requirements of "Building Seismic Design Code" (GB50011-2010)[22] and "Building Energy Dissipation and Vibration Reduction Technical Code" (JGJ 297-2013)[23].

2.2. Design of the sub-structure

To investigate the seismic performance of a BRBF with HSCFSSTC and H-shaped steel beam, a single-story single-span specimen containing BRBs was selected from the bottom of the prototype structure as a sub-structure, and pseudo-static tests under cyclic loading were conducted.

The specimens were designed and processed at a 1/3 scale according to the prototype frame, with specimen numbers SP1-Test and SP2-Test. The schematic diagrams and key cross-sectional dimensions are shown in Figs. 2-5. In the SP1-Test frame, the BRB (referred to as BRB1) was connected to the beam-column using butt welds, while in the SP2-Test frame, the BRB (referred to as BRB2) used pin connections, with all other parameters remaining the same. Steel beams are connected to CFST columns through external flange plates, the width of which is designed according to FEMA-350 [24], and references for design and calculation of BRB and frame angles and ribs are given in [25, 26].

To secure the test frame, a steel beam with high rigidity was welded at the bottom of the column. The detailed parameters of the beams, columns and BRBs are shown in Table 1.

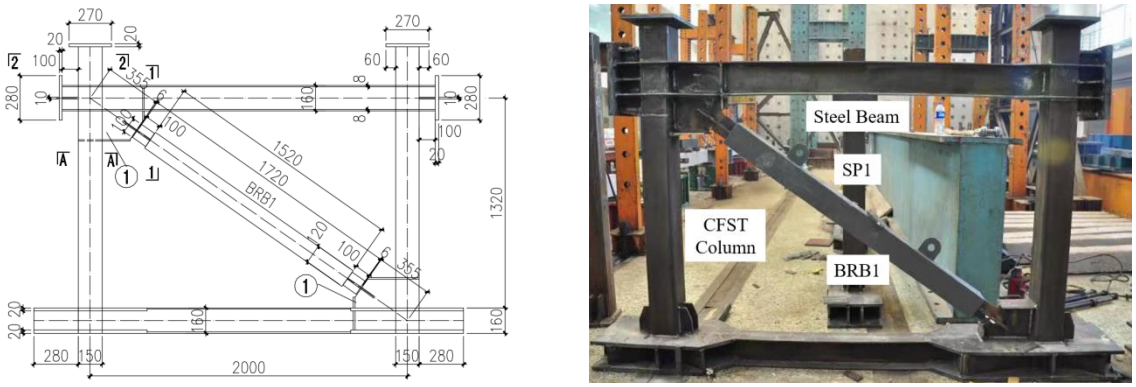

Fig. 2 Schematic diagram of specimen SP1

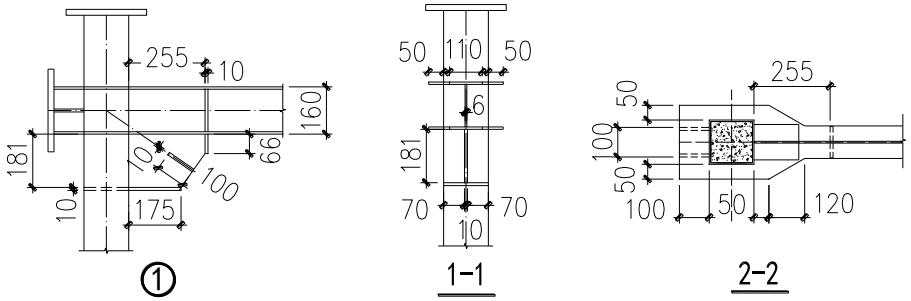

Fig. 3 Key cross-sectional dimensions of specimen SP1

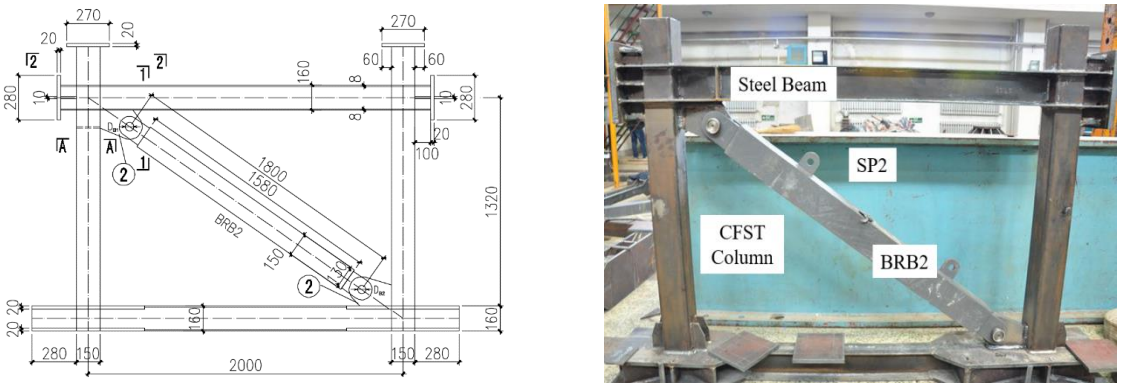

Fig. 4 Schematic diagram of specimen SP2

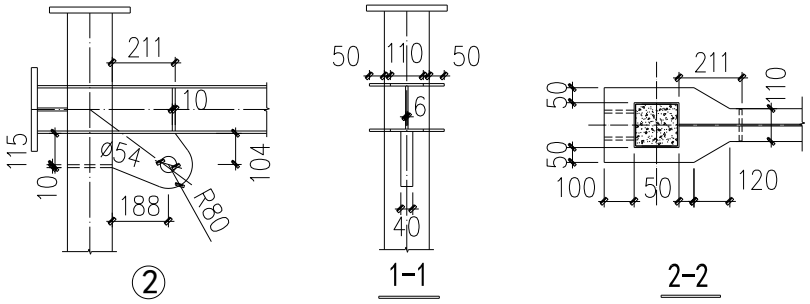

Fig. 5 Key cross-sectional dimensions of specimen SP2

Table 1
Frame design parameters of specimens

Specimen number	SP1	SP2
Connection method of BRB with beam and column	Butt-welded connection	Pin connection
Column (cold-formed square steel tube Q460)	□150×150×5 mm	□150×150×5 mm
Concrete strength grade	C100	C100
Specimen length, width	2000×1400	2000×1400
Beam (Q345)	H-160×110×6×8mm	H-160×110×6×8mm

2.3. Specimen parameters

The buckling-restrained braces of the test specimens were designed and manufactured by Shanghai Lanke Building Damping Technology Co., Ltd., and were designed to bear 60% of the total shear force of the frame. The core segment of the BRB was made of Q235 steel, while the transition segment were made of Q345 steel. The transition segment of the BRB1 specimen utilized a cross-shaped plate that was connected to the frame using double-sided fillet welds, while the BBR1 itself was connected to the gusset plate via butt fusion welds. In addition, the inner partition is welded to the end column of the pinch plate, and the reinforcing rib is welded to the supporting column to strengthen the stress concentration area and prevent premature failure of the node area. The BRB2 is mounted on the 40mm thick gusset plate with steel shafts. The gusset plate was connected to the column and the beam of the frame using fusion welds, and an internal partition was welded inside the column at the gusset plate end, with stiffeners welded on the beam web. The specific parameters of the BRBs are shown in Table 2.

Table 2
Design parameters of BRB

Number	BRB1	BRB2
BRB total length (L_1)	1720	1930 (center-to-center distance of holes1800)
BRB restrained segment length (L_2)	1580	1600
BRB core segment length (L_3)	1120	1120
BRB transition segment length (L_4)	300	405
Cross-sectional dimensions of BRB transition segment (Q345)	+100×100×10 mm	=130×25 mm
Cross-sectional dimensions of BRB restrained segment (Q345)	□120×120×10 mm	□150×120×10 mm
Cross-sectional dimensions of BRB core segment (Q235)	-41×25 mm	-41×25 mm
A_{gsc} (mm^2)	1025	1025
ϖ	1.5	1.5
β	1.15	1.15
P_y (kN)	261	261
ϖP_y (kN)	392	392
$\varpi\beta P_y$ (kN)	450	450
Hole diameters of BRB transition segment D_{B1}, D_{B2}	-	54
Pin diameters D_1, D_2	-	53.5
Hole diameters of BRBF gusset plate D_{E1}, D_{E2}	-	54

β= BRB compression strength adjustment factor; ϖ=BRB tension overstrength factor; P_y=axial yield load

The columns used cold-formed steel tubes filled with C100 concrete. The concrete cubic compressive strength recorded during testing was 97.1MPa. The steel beams were fabricated by welding, and the connection between the beams and columns was made using external plate welding method. In addition, a column cap made of 20 mm thick steel plate is welded to each column. The strength of the steel in the specimen was determined by tensile tests, which were conducted in accordance with the "Metal Materials Room Temperature Tensile Test Method" (GB/T 228-2002)[27], and the yield strength, tensile strength of the BRB yielding section, gusset plate, steel tube, and steel beam web and flange are presented in Table 3.

Table 3
Material properties of specimens SP1 and SP2

Steel type	f_y (material yield strength)	f_u
Steel tube (Q460)	434.6	543.7
Beam flange (Q345)	349.6	497.3
Beam web (Q345)	356.4	508.5
BRB core steel (Q235)	254.5	422.8
Gusset plate (Q345)	371.3	515.2

2.4. Test device and measurement scheme

The tests were finished at the structural laboratory of Shenyang Jianzhu University. The test loading device is illustrated in Fig. 6. A steel beam with high stiffness was welded to the bottom of the SP1-Test and SP2-Test columns. Prior to the test, the specimens were secured on the rigid ground using four steel beams with high stiffness and ground anchor bolts. During the test, two hydraulic cylinders exert an axial force of 400 kN on the top of the test structure. The jacks were affixed to the rigid crossbeam of the reaction frame through free sliding supports, which allowed simultaneous movement with the column when applying horizontal displacement. The end of the beam, which was fastened to the loading end plate of the beam, received horizontal displacement from an MTS actuator. The actuator had a maximum loading capacity of 500kN and a stroke of ±250mm. The test device is shown in Fig. 7.

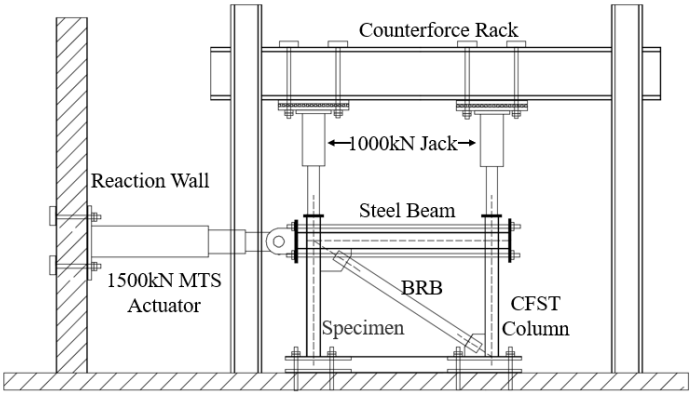

Fig. 6 Schematic diagram of test loading device

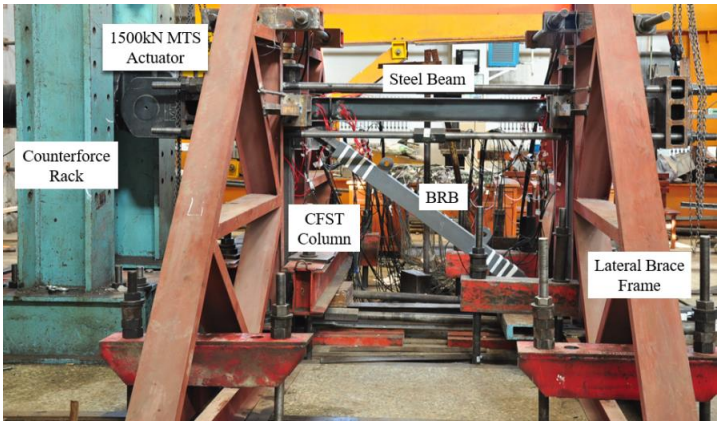

Fig. 7 Test loading device

Steel trusses were positioned on both sides of the specimen and secured to the rigid ground. To prevent out-of-plane instability of the specimen during the test procedure, a sliding device was inserted between the specimen and the steel trusses, with the top support placed at the junction of the beam and column of the test frame.

The test measurements consisted of three parts: load, displacement and strain. The configuration of strain gauges and displacement meters during the test is shown in Fig. 8. The horizontal reaction force and horizontal displacement of the test frame were automatically recorded by the MTS actuator. To measure the strain values of the beam and columns of the test frame, strain gauges were fastened to the bottom of the columns, the core area of the beam-to-column joint, the upper and lower flanges, and the web of the beam sections. At the two ends of the specimen, displacement meters W3 and W4 measured the axial displacement of the BRB, and the average value of the two measurements served as the axial displacement. Strain gauges were attached along the axial direction of the BRB yielding section and the exposed connection portion to measure the strain values. The loading displacement was controlled by the displacement meter W1 arranged at the beam end. During the experiment, all test instruments were synchronized with the MTS system for data acquisition.

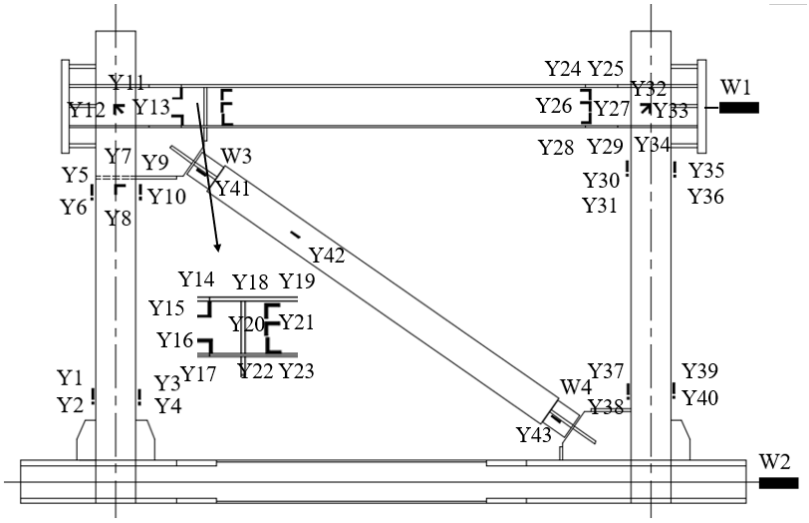

(a) SP1 strain gauge and displacement meter layout

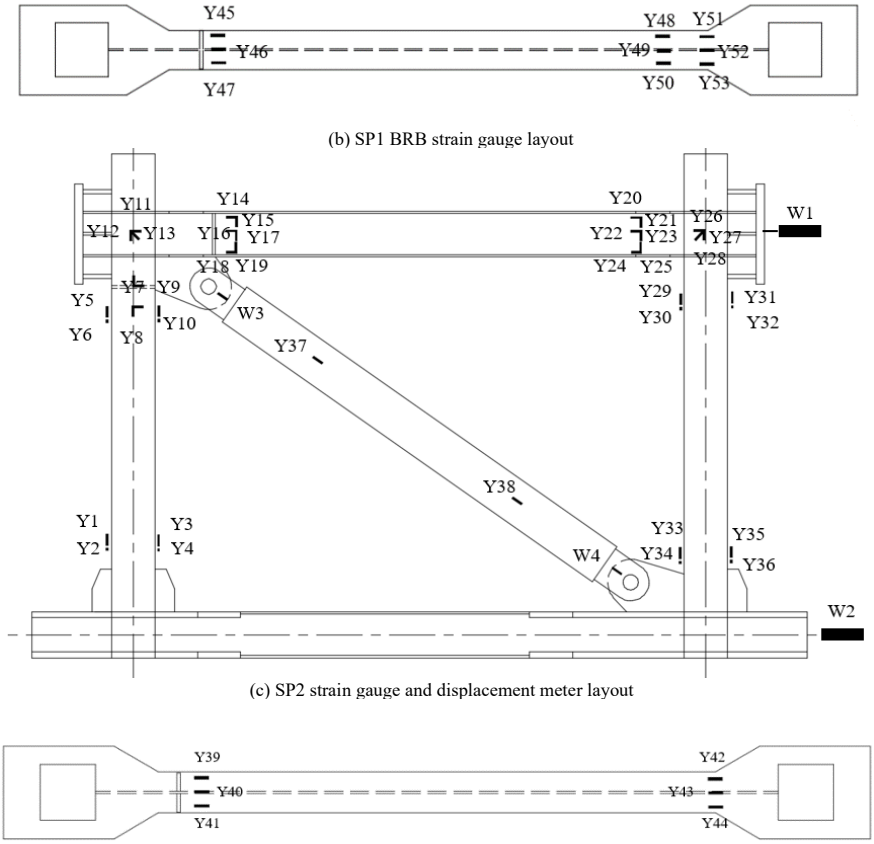

(b) SP1 BRB strain gauge layout

(c) SP2 strain gauge and displacement meter layout

(d) SP2 BRB strain gauge layout

Fig. 8 Specimen strain gauge and displacement meter layout

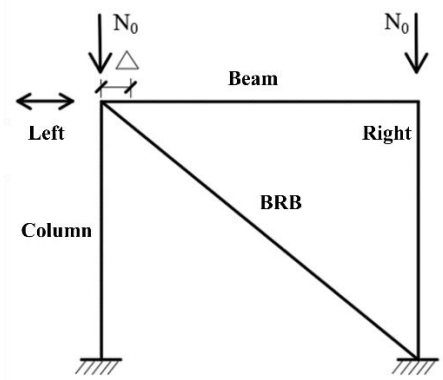

Fig. 9 Test loading schematic

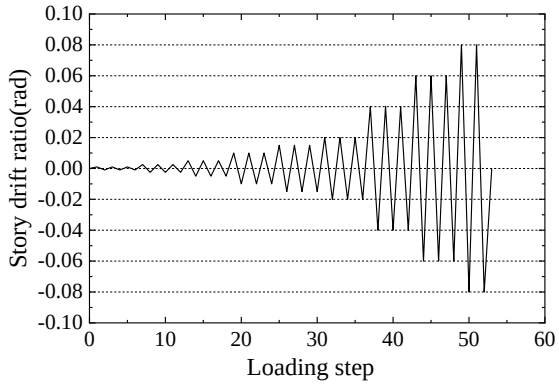

Fig. 10 Test loading procedure

2.5. Loading protocol

The test loading protocol followed the specifications outlined in the American Institute of Steel Construction (AISC) 2010 standard[25]. The loading schematic is presented in Fig. 9, and the test loading procedure for displacement control is seen in Fig. 10. The test was conducted using displacement control, with $\triangle_1$=±1.4mm (θ_1=0.001rad); $\triangle_2$=±3.5 mm (θ_2=0.0025 rad); $\triangle_3$=±7 mm (θ_3=0.005rad); $\triangle_4$=±14 mm (θ_4=0.01 rad); $\triangle_5$=±21 mm (θ_5=0.015 rad); $\triangle_6$=±28 mm (θ_6=0.02 rad); $\triangle_7$=±56 mm (θ_7=0.04 rad); $\triangle_8$=±84 mm (θ_8=0.06 rad) for three cycles; $\triangle_9$=±112 mm (θ_9=0.08 rad); $\triangle_{10}$=±140 mm (θ_{10}=0.1 rad) for two cycles. The loading continued until the specimen became unstable and failed, or until the load decreased to 85% of the ultimate load. It should be noted that $\triangle=\theta\times h$.

3. Test phenomena and failure characteristics

3.1. Experimental observations

3.1.1. Specimen SP1-Test

The Finite Element Simulation stress units in Figs. 11and 13 are MPa, Strain unit dimensionless.

When loading the specimen, it is specified that loading to the left side is positive loading. At the first cycle of the 7th loading level (4% rad), the positive loading reached 40mm (2.9% rad), causing yielding on the left side of the beam noticeable buckling of the lower flange, as shown in Fig. 11c. When the loading reached 45mm (3.2% rad), the upper flange of the right side of the beam buckled, as shown in Fig. 11c. At a loading of 56mm (4% rad), web buckling was observed at both ends of the beam. Additionally, the left column (referred to as column SP1-T-left) displayed local buckling at the base of the steel tube, as illustrated in Fig. 11i. The right column (referred to as column SP1-T-right) experienced local buckling at the steel tube near the end of the BRB1 gusset plate. When the negative loading reached -50mm (-3.6% rad), local buckling appeared on the steel tube beneath the left column joint, as shown in Fig. 11c. After the test, the steel pipe was cut and some cracks were found in the left column joint concrete, and the concrete at position 1 on the right side was locally broken, as shown in Fig. 11e.

During the first cycle of the 8th loading level (6% rad), the negative loading reached -65mm, causing out-of-plane instability of the beam. The right loading was stopped, and the negative left loading was completed for the first cycle of the 8th loading level. After the first cycle, a non-through crack measuring 0.5mm in width and 7mm in length was found on the outer side of the joint weld where BRB1 was connected to the right column gusset plate, as shown in Fig. 11h. To measure the ultimate load of specimen SP1, the second cycle of the 8th loading

level was continued. The specimen was loaded to the right up to 65mm and then the left up to -66mm (-4.6% rad). At this point, the load dropped sharply to around 400kN (55% of the maximum load). A loud "bang" sound was heard, and although the displacement continued to increase slightly, the horizontal load did not increase. It was concluded that the core reinforcement of BRB1 could break due to tensile loading, which would cause BRB1 to lose its load-bearing capacity, so the tests were stopped.

After the test, the Steel Casing of BRB1 and the columns were cut open. Observations from the images of the cut-open BRB1 revealed that its core segment experienced both compressive buckling and tensile fracture during the test, confirming that the core steel was broken under tension at around -66mm (-4.6% rad) as depicted in Figs. 12a, b and c. After inspecting the beam, column and BRB1 joint area, no cracks or crushing damage in the concrete were found (see position 2 in Fig. 11e). The gusset plate and stiffeners increased the stiffness of the joint, thereby preventing any yielding or failure in this area throughout the loading process. It can be seen from Figs. 11i to 11p that the concrete damage at the base of the left column SP1-T-left was more severe than that at the base of the right column SP1-T-right.

3.1.2. BRB1 test observations

Prior to loading to 6% rad, no cracks were observed in the joint weld connecting the ends of BRB1 to the gusset plates. However, during the second cycle at 6% rad, a non-through crack measuring 0.5mm wide and 7mm long was found on the outer side of the joint weld where BRB1 was connected to the column SP1-T-right gusset plate, as shown in Fig. 11h. Throughout the entire test, no apparent yielding or failure phenomena such as cracking in welds, local buckling or out-of-plane instability was observed in the laminated panels tested in SP1.

During the test, when the SP1-Test 's horizontal displacement reached -3.2mm (or an story drift angle of-0.23% rad), the axial displacement of BRB1 reached -2.1mm (with negative displacement indicating tension in BRB1), causing BRB1 to yield under tension. The axial displacement of BRB1 was measured using displacement sensors fixed at the transition segments of BRB1, and the yielding of BRB1 was determined using strain gauges attached to the yielding section of BRB1. The yield load of BRB1 under tension was 265kN, which is close to its design yield load of P_y = 261kN, calculated using the strain values from the strain gauges attached to the connection portions of BRB1. When the horizontal displacement reached 3.6mm to the right (or an story drift angle of 0.26% rad), the axial displacement of BRB1 reached 2.2mm, causing BRB1 to yield under compression. The corresponding yield load was 274kN, which is 5% higher than the design yield load of P_y = 261kN. Moreover, the compressive yield load-bearing capacity of BRB1 was 3% higher than the tensile yield load-bearing capacity.

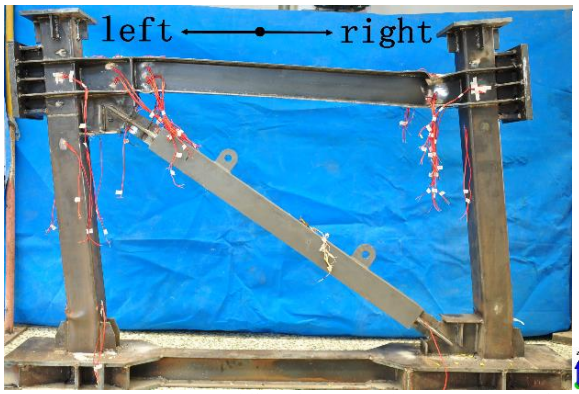

a. Post-test failure phenomena of SP1-Test

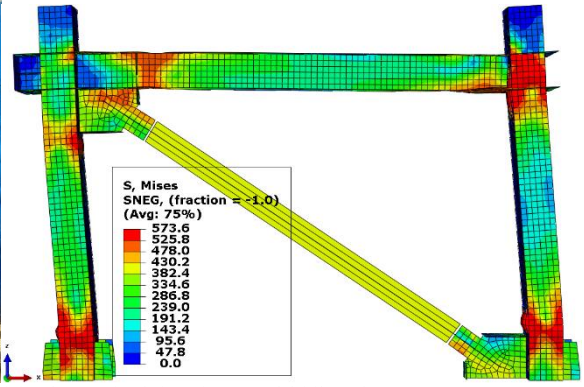

b. Finite element simulation of SP1-Model failure phenomena

c. Left-side beam-column joint (test)

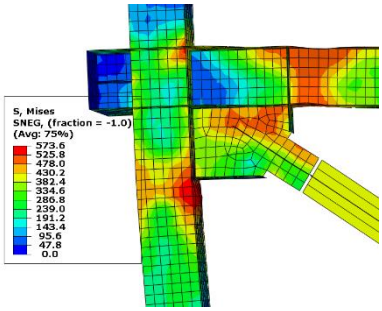

d. Left-side beam-column joint (FEM)

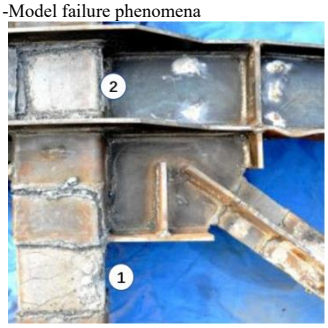

e. Left-side beam-column joint concrete

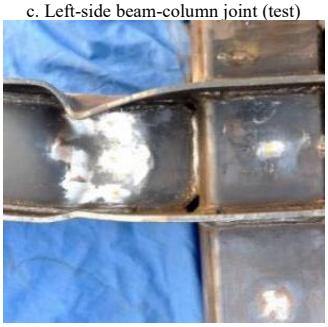

f. Right-side beam-column joint (test)

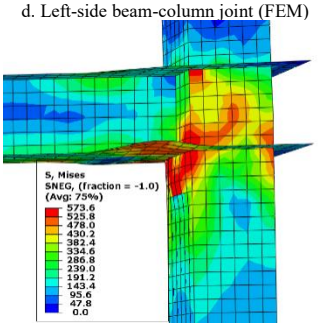

g. Right-side beam-column joint (FEM)

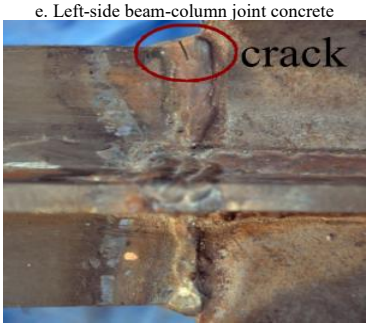

h. Crack in BRB1 butt-weld

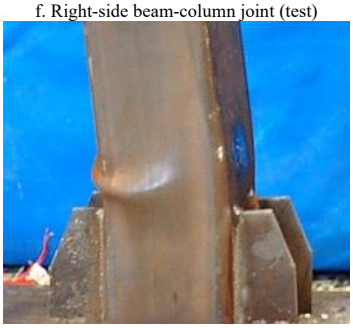

i. Left-side column base (test)

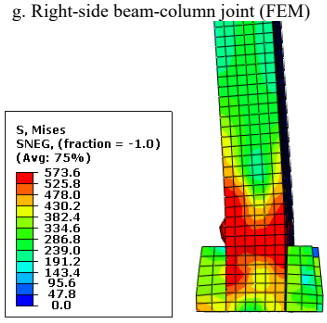

j. Left-side column base (FEM)

k. Left-side column base concrete

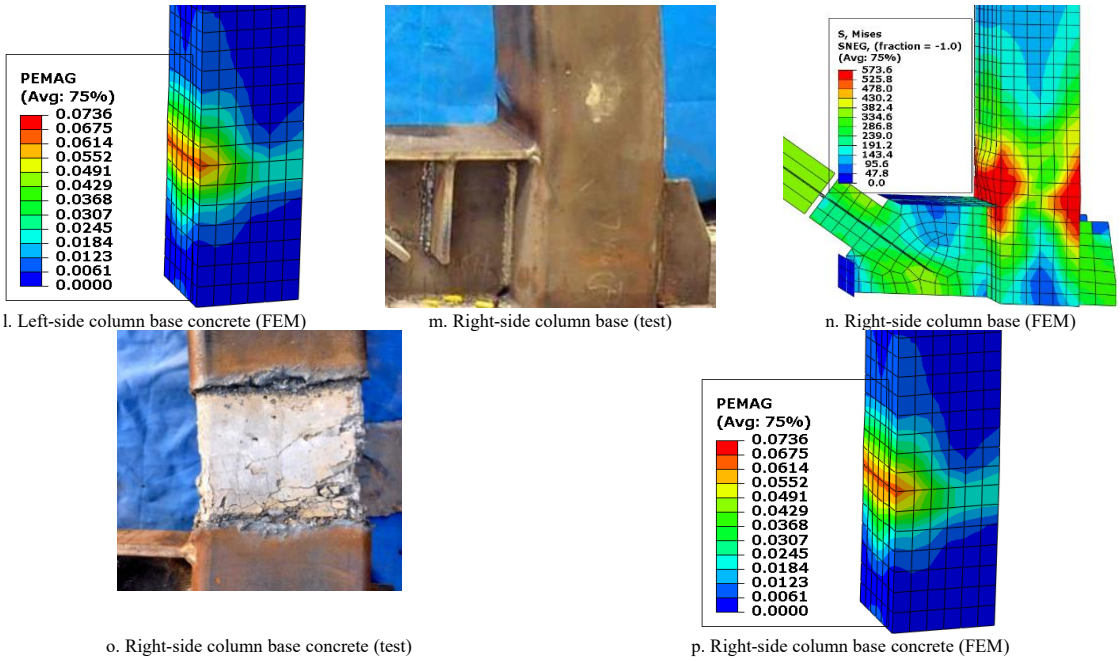

l. Left-side column base concrete (FEM) m. Right-side column base (test) n. Right-side column base (FEM)

o. Right-side column base concrete (test) p. Right-side column base concrete (FEM)

Fig. 11 Failure phenomena of specimen SP1

a. BRB1 core segment b. Core segment fracture c. Core segment buckling

Fig. 12 Failure phenomena of BRB1

3.1.3. Specimen SP2-Test

Following the loading protocol, displacement loading was carried out incrementally. At the first cycle of the 6th load level (2% rad), when the forward load reached about 28 mm (2% rad), local buckling happened at the lower flange of the left end of the beam, as shown in Figs. 13c and 13d. Additionally, local buckling was observed at the lower flange of the right end of the beam, as shown in Figs. 13e and 13f.

During the first cycle of the 7th loading level (4% rad), as the positive loading reached 35mm (2.5% rad), the upper flange and web of the beam at the left end, where it connected to BRB2, buckled as shown in Fig. 13c. The buckling of the right end of the beam also occurs at the flange and web (see Fig. 13e). The steel plate of the column connected to the lower flange of the beam experienced tensile buckling and delamination from the concrete, as shown in Fig. 13e. When the load is -42mm (-3%rad) to the left, the weld of the outer flange plate at the right end of the beam and the column cracks, causing deformation of the lower flange at the right end of the beam and the beam becomes more pronounced. Furthermore, the web of the beam buckled, and the base of the left column of specimen SP2-Test (referred to as column SP2-left) experienced bulging, as shown in Figs. 13h and 13i. Simultaneously, the steel plate at the base of the right column of specimen SP2 (referred to as column SP2-T-right) buckled, as depicted in Figs. 13j and 13k.

During the first cycle of the 8th loading level (6% rad), when the loading reached 42mm (3% rad) to the right, out-of-plane instability occurred in the beam, and the loading to the right was stopped. To determine the maximum load when loading to the left, the loading was continued to the left. When the loading reached 84mm (6% rad), no evidence of tensile rupture in the core segment of BRB2 was observed. At this point, there was no need to continue loading, and the loading was immediately stopped. The test of specimen SP2-Test was concluded. Throughout the entire test, no cracks or fractures were observed in the butt weld joint between BRB2 and the gusset plates.

3.1.4. BRB2 failure behavior

During the testing process, when the load was applied to the right and reached a displacement of about 5.6mm (0.4%), BRB2 underwent compressive yielding, resulting in an axial displacement of 1.8mm. The yielding force was measured to be approximately 273kN, which is 5% higher than the design value P_y=261 kN. Similarly, when the load was applied to the left and reached a horizontal displacement of about -6mm (-0.43%), BRB2 underwent compressive yielding, resulting in an axial displacement of -1.9mm. The yielding force was measured to be approximately 280kN, which is 7% higher than the design value P_y=261 kN. The axial displacements at which BRB2 experienced tensile and compressive yielding were relatively close, and the differences in the yielding forces were not significant. The methods used to determine the yielding of BRB2, as well as to obtain its axial displacement and yielding force, were consistent with those for BRB1. Additionally, no cracks or fractures were observed in the butt welds between BRB2 and the gusset plates throughout the testing process.

3.2. Comparison of test observations between specimens SP1-Test and SP2-Test

The results of specimen SP2-Test showed that the steel beam exhibited earlier yielding and buckling failure occurred at both ends of the steel beam, compared to the same locations in specimen SP1-Test. Comparing the yield buckling behavior of the left and right flanges of the sp2 test and the sp1 test steel beam, the left flange of the sp2 test steel beam buckling buckling failure occurs at the lower deflection angle of 2.0% rad, while the sp1 test lags behind at 2.9% radian. Likewise, in the sample sp2 test, the right flange of the steel beam buckled and formed a plastic hinge at a story dip of 2.1% rad; while for the SP1 test sample, this occurred at a higher story drift angle of 3.2% rad.

From Figs. 11 and 13, it can be seen that the damage at the left end of the steel beam in specimen SP2-Test is much more severe than that in specimen SP1-Test. Fig. 13g provides a clear illustration of the damage observed in specimen SP2-Test. It can be seen from the figure that when the sample reaches the sheet deflection angle of 2.9% rad, cracks appear in the weld seam between the outer plate of the right lower flange and the column. When the load was increased to 3.3% rad, the outer plates connecting the bottom flanges of the steel beams fractured. During the test, specimen SP1-tested steel beam formed a plastic hinge at both ends and no weld cracking or plate tearing occurred.

The testing process demonstrated that the failure at both ends of the steel beam in specimen SP2-Test occurred earlier than in specimen SP1-Test, and the

extent of the damage was more severe in specimen SP2-Test. Instability out-of-plane happened earlier in the specimen SP2-test than in the specimen SP1-test.

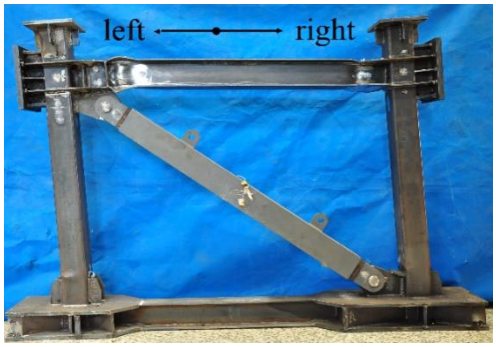

(a) Damage phenomenon of SP2-Test after the experiment

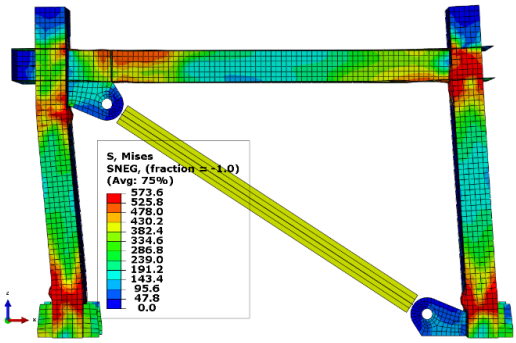

(b) Finite element simulation of SP2-Model damage phenomenon

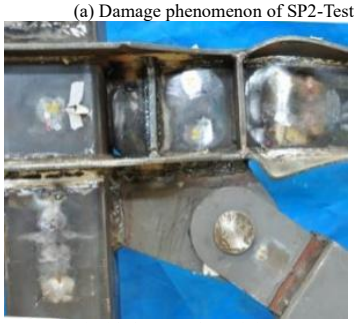

(c) Left-side beam-column joint (test)

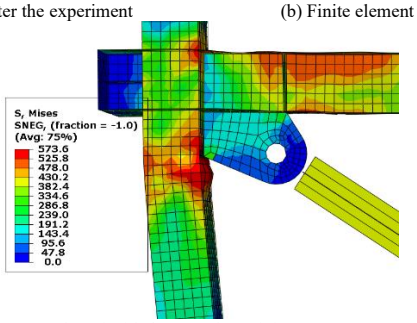

(d) Left-side beam-column joint (FEM)

(e) Right-side beam-column joint (test)

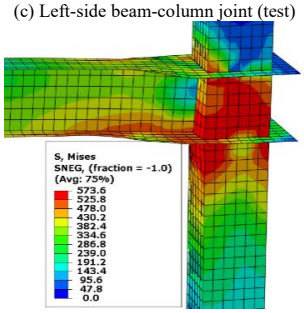

(f) Right-side beam-column joint (FEM)

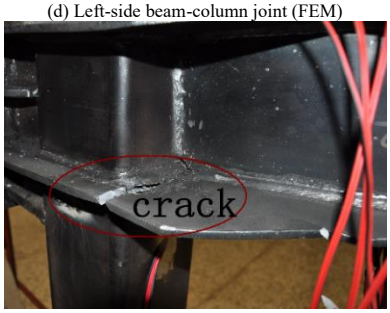

(g) Crack in the lower flange weld of the right-side external plate

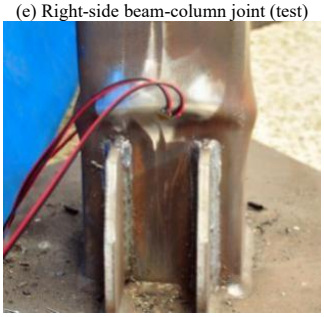

(h) Left-side column base (test)

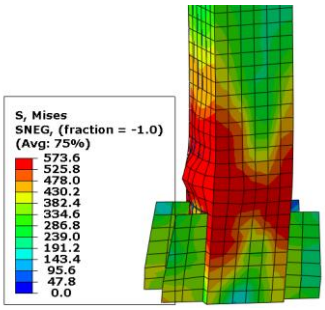

(i) Left-side column base (FEM)

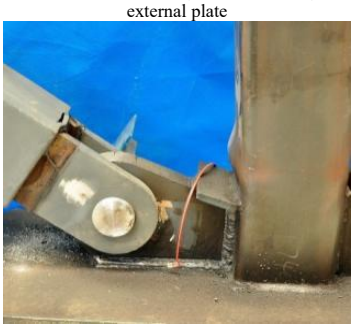

(j) Right-side column base (test)

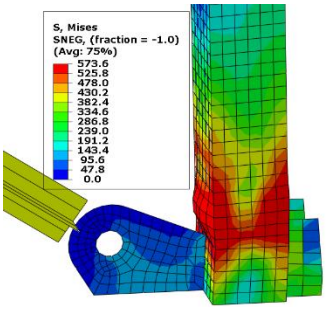

(k) Right-side column base (FEM)

Fig. 13 Failure Phenomenon of Specimen SP2

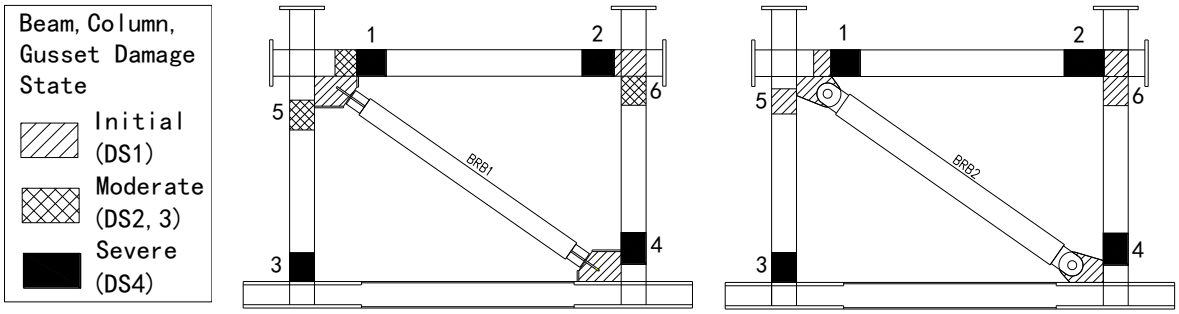

(a) Specimen SP1-Test (b) Specimen SP2-Test

Fig. 14 Schematic of the plastic hinge location during the specimen test process

As shown in Figs. 11 and 13, the left column of the specimen SP1-Test exhibited yielding and plastic hinge formation at the lower portion of the gusset plate, accompanied by the appearance of cracks within the concrete of the steel tube. Contrary to the behavior of the left column in the specimen SP1-test, the left column of specimen SP2-Test did not yield or form a plastic hinge in the same area, suggesting that the pin connection is beneficial in mitigating the bending moment transferred from the BRB transition segments to the column. Nevertheless, according to the test results, the overall stress distribution and damage of specimen SP1-test were significantly better than that of specimen SP2-test.

Fig. 14 illustrates the progression of yielding, plastic hinge formation, and damage extent and location in the beams, columns, gusset plates and other components of specimens SP1-Test and SP2-Test throughout the testing process. Initially, plastic hinges develop at the ends of the beams with BRB connections and subsequently at the ends of the beams without BRB connections. Subsequently, plastic hinges appear on column bases without BRB connections and finally on column bases with BRB connections. During the whole test process, the beam-to-column connection and the core area of the BRBF gusset plate were not damaged and were in an elastic state.

4. Analysis of experimental results

4.1. Hysteresis curves

The hysteresis curves for specimens SP1-Test and SP2-Test are illustrated in Fig. 15. Both specimens exhibited full hysteresis loops, with no pinching phenomena detected, and the ultimate load capacities for both specimens are relatively close. While the curve for specimen SP1-Test remains consistently smooth, the curve for specimen SP2-Test demonstrates an abrupt transition in proximity to the zero load, as indicated by the 'pin slip' in Fig. 15b. Upon further analysis, this sudden change observed in the test results can be attributed to two primary factors. Firstly, prior to the tests, measurements were taken of the gusset plate hole diameters and pin shaft diameters of BRB2. The pin shaft diameters were found to be approximately 0.7mm smaller than the BRBF connection gusset plates hole diameters, resulting in a gap between them. Consequently, when the core segment of BRB2 changed from compression to tension, or vice versa, it was almost unloaded, and the horizontal load was entirely supported by the beam and columns. Secondly, to facilitate the installation of BRB2, there was a clearance of approximately 1.0 mm between the two connecting plates of BRB2. When the frame was loaded in the positive direction, this gap caused BRB2 to undergo minor out-of-plane deformations, which affected the effective transfer of horizontal loads to BRB2.

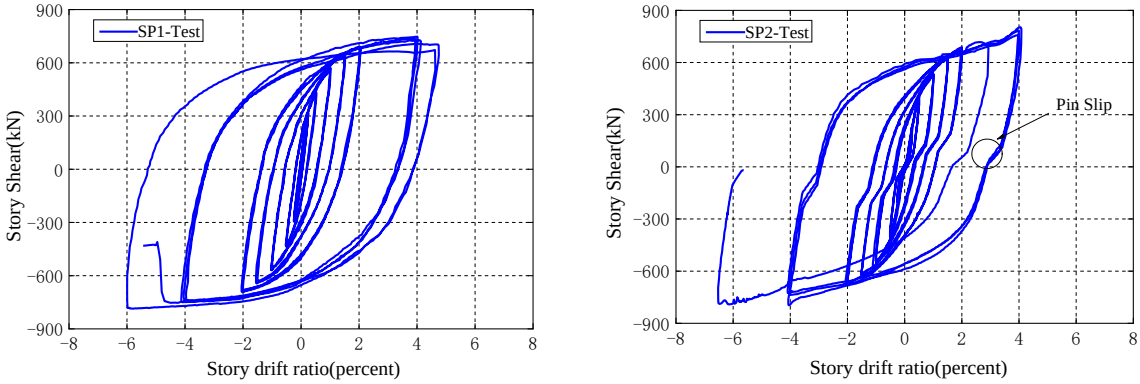

（a）SP1-Test （b）SP2-Test

Fig. 15 Load-Displacement Curve of the Test Specimen

4.2. Energy dissipation

In order to evaluate the energy dissipation capacity of the test specimen, this paper introduces two parameters: the equivalent viscous damping coefficient, denoted as ζ_e, and the energy dissipation coefficient, denoted as E. The expressions for the equivalent viscous damping coefficient ζ_e and energy dissipation coefficient E of the hysteresis loop, as converted based on Fig. 16, are shown below.

$$\zeta_e = \frac{1}{2\pi} \cdot \frac{S_{ABC}+S_{CDA}}{S_{\Delta OBE}+S_{\Delta ODF}} \tag{1}$$

$$E = 2\pi\zeta_e \tag{2}$$

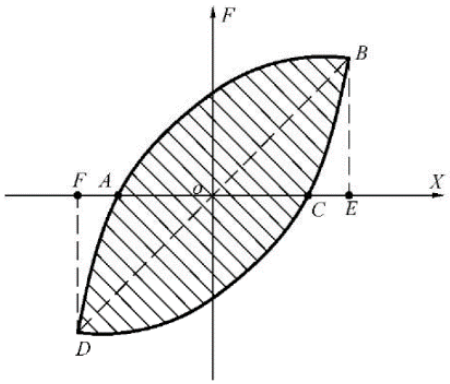

Fig. 16 Percentage of shear force carried by the BRB (experiment)

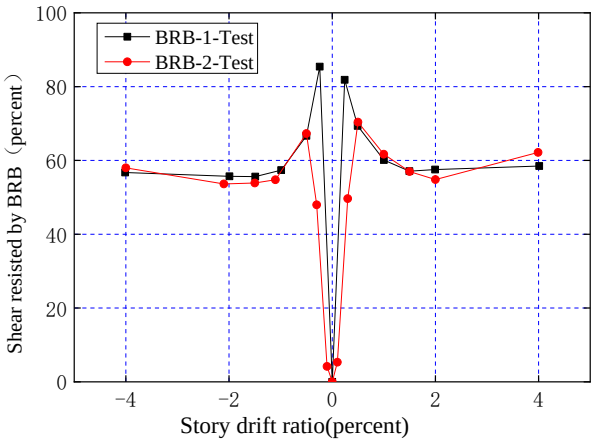

Fig. 17 Percentage of Shear Force Carried by BRB (experiment)

Table 5
Energy dissipation indicators of specimens

Specimen ID	Total energy dissipation (kN·mm)	Equivalent viscous damping coefficient ζ_e	Energy dissipation coefficient E
SP1	569177	0.349	2.192
SP2	487415	0.299	1.878

Using Equations (1) and (2), the total energy dissipation, equivalent viscous damping ratio ζ_e, and energy dissipation ratio E of each specimen at the ultimate state can be calculated, as presented in Table 5. The total energy dissipation, equivalent viscous damping ratio ζ_e, and energy dissipation ratio E of specimen SP1-Test with welded connections are all greater than those of specimen SP2-Test with pin connections.

4.3. Energy-dissipation capacity of BRB

The shear force ratios of BRB1 and BRB2 during the testing process are illustrated in Fig. 17. It is observed that under rightward loading, when the story

drift angle increases from 0 to 0.5% rad, a substantial difference exists between the shear forces carried by BRB1 and BRB2. As the inter-story displacement angle increases from 0 to 0.25 % rad, the proportion of shear force borne by BRB1 to the total frame shear force increases from 0 % to a peak of about 82%. In this phase, the axial load of BRB1 exhibits a linear relationship with the story drift angle, and BRB1, in both tension and compression begins to yield when the story drift angle approaches 0.25% rad.

After exceeding 0.25 % rad inter-story displacement angle, the proportion of horizontal shear force borne by BRB1 to the total frame shear force decreases as the inter-story displacement angle continues to increase. As the inter-story displacement angle increases from 0 to 0.5 % rad, the proportion of shear force borne by BRB2 to the total frame shear force increases from 0 % to a peak of about 70 %. At an angle of interlaminar displacement of 0.5 % rad, BRB2 starts to yield in both tensile and compressive states. When the inter-story displacement angle exceeds 0.5 % rad, the proportion of horizontal shear force borne by BRB2 to the total frame shear force decreases with the increase of inter-story displacement angle. Moreover, within the range of 0.5% to 4% rad story drift angle, the shear forces carried by both BRB1 and BRB2 contribute to approximately 60% of the total story shear force, which is in relatively close agreement with the design expectation. In the initial loading stage (0 to 0.3% rad), gaps between the connecting pin shafts, gusset plate holes and BRB2 connecting plate holes prevent the effective transmission of shear force to BRB2 during low loading displacements. As a result, the shear force carried by BRB2 is minima during this initial loading stage, leading to a significant deviation from the ideal state.

The energy dissipation capacity of buckling-restrained braces can be evaluated through the cumulative ductility demand μ_c, as specified in AISC (2010) [25].

$$\mu_{max}=\Delta_{max}/\Delta_{by} \quad (3)$$

$$\mu_c=(\sum\Delta_{plastic})/\Delta_{by} \quad (4)$$

in which, $\sum\Delta_{plastic}$ represents the cumulative plastic deformation of the BRB, and Δ_{max} represents the maximum deformation of the BRB.

When the story drift of specimen SP1-Test reached 4% rad, the maximum ductility demand of BRB1 μ_{max} was 21, the cumulative ductility demand μ_c was 518.2, which was comparable to the value reported in reference [8]. The cumulative ductility demand μ_c increased to 671.2 at the point of BRB1 tensile fracture, which exceeded the value reported in reference [8]. It also surpassed the requirement of cumulative ductility demand μ_c greater than 200 specified in AISC (2010) [25].

When the story drift of specimen SP2-Test reached 4% rad, the maximum ductility demand of BRB2 μ_{max} was 20.8, which was comparable to the value reported in reference [8]. The cumulative ductility demand μ_c was 406.6, which was lower than the value reported in reference [8], but it still exceeded the requirement of cumulative ductility demand μ_c greater than 200 specified in AISC (2010) [25].

5. Finite element simulation

5.1. Constitutive model of materials

The steel model for columns and beams is an ideal bilinear model without accounting for strain hardening. The plastic damage model defined in ABAQUS is used for concrete materials, and the stress-strain relationship is calculated using the material model [28] proposed in the literature, while considering the confinement effect of steel pipes on the concrete core. For the BRB core, the steel material model uses the Combined Hardening model in ABAQUS, which considers both isotropic hardening and kinematic hardening. The specific parameters are determined based on reference [29].

5.2. Element types and meshing

The meshing of the specimen is shown in Fig. 18. The steel tubes, H-shaped steel, stiffeners and the BRB are modeled using S4R shell elements. The column grid is 25 mm, the beam grid is 25 mm, and the grid on the gusset plates and stiffeners is 20 mm. Chung-Che Chou and Jia-Hau Liu [30] modeled the BRB core using truss elements T3D2 (two-node) to avoid core buckling,in order to eliminate the BRB restraining members from the model. Tsai KC [19]and Yu YJ [31] recommend that the BRB of frame can be conveniently replaced by a truss element in a BRBF analytical model. The BRBs were modeled by Li Jiaqi [32] using S4R shell elements which the out-of-plane displacement is set to zero to avoid core buckling.In this paper, the BRBs are modeled using S4R shell elements. The number of elements for the BRB core along the length direction is set to one to avoid core buckling. The concrete is modeled using C3D8R eight-node linear hexahedral elements. The contact relationship between concrete and steel pipe is defined as normal hard contact. Considering tangential friction, the Coulomb coefficient of friction is 0.6 [33]. The sample SP1 model (scaled finite element model of SP1 test) uses connection constraints to connect the BRB to the frame, and the sample SP2 model (scaled FE model of SP2 tests) uses hinge constraints for pin connections and gussets are relative in the plane of the frame rotate.

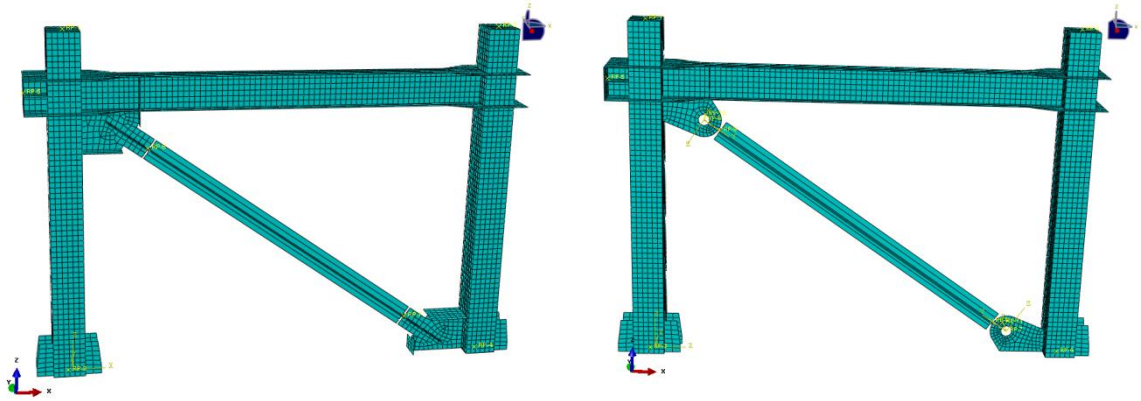

(a) Schematic diagram of mesh division and contact relationship for SP1-Model

(b) Schematic diagram of mesh division and contact relationship for SP2-Model

Fig. 18 Mesh division of test specimens

5.3. Model boundary conditions and loading method

The finite element model has the same boundary conditions as the test frame, the bottom of the column is fixed, the vertical concentrated force is applied at the top of the column during the simulation, as shown in Fig. 9 (test loading diagram). During the test, the lateral support is used to limit the out-of-plane instability of the specimen, the out-of-plane horizontal displacement at the top of the column is set to zero during the simulation.

Furthermore, the loading method is in alignment with the test frame, the in-plane horizontal displacement was loaded at the left end of the beam , with each level of loading displacement and number of cycles consistent with the test frame loading method.

5.4. Comparison and analysis of experiment and finite element results

As can be seen from Figs. 19-23, the finite element simulation results of the specimen SP1-model show excellent agreement with the experimental results. However, the hysteresis loop shape of the finite element simulation results for specimen SP2-Model slightly deviates from the experimental results, primarily due to the unaccounted processing errors in the pin shaft diameter and gusset plate hole diameter of BRB2 during modeling. Nevertheless, as shown in Fig. 23, the backbone curve of the SP2-model agrees well with the results of the experiment.

Based on the results of experiments and simulations (refer to Figs. 17 and 24), the shear force ratios of BRB1 and BRB2 remain very close throughout the entire loading period. As the story drift angle increases from 0 to ±0.25%, the

shear force ratios of BRB1 and BRB2 rise from 0 to a maximum value of 80%. For the inter-story displacement angles between 0.25 % and 1.5 % and between - 0.25 % and -1.5 %, the proportion of the horizontal shear force borne by BRB1 and BRB2 to the total shear force of the frame decreases with the increase of the inter-story displacement angle. Finally, when the story drift angle falls within the range of 1.5% to 4% and -1.5% to -4%, the shear force ratios of BRB1 and BRB2 are within the interval of 55-60%.

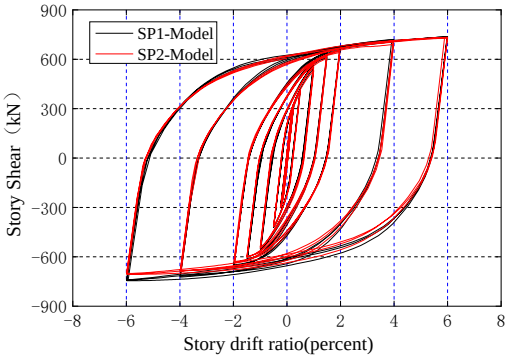

Fig. 19 Load-displacement curves of the specimens (FE simulation)

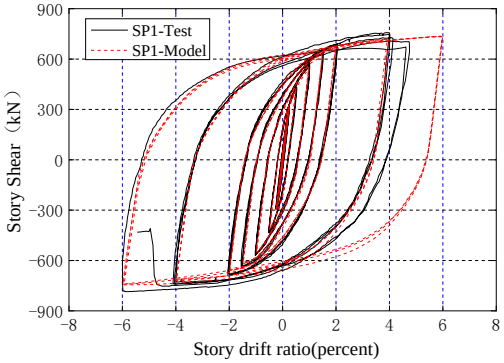

Fig. 20 Load-displacement relationship of specimen SP1

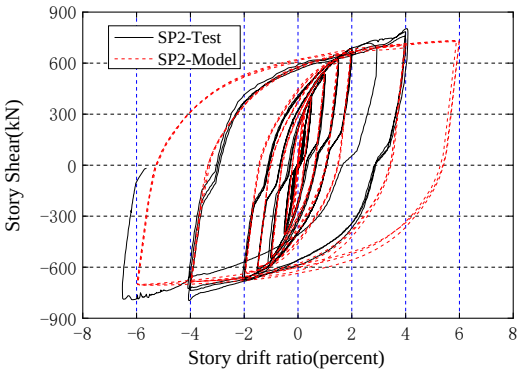

Fig. 21 Load-displacement relationship of specimen SP2

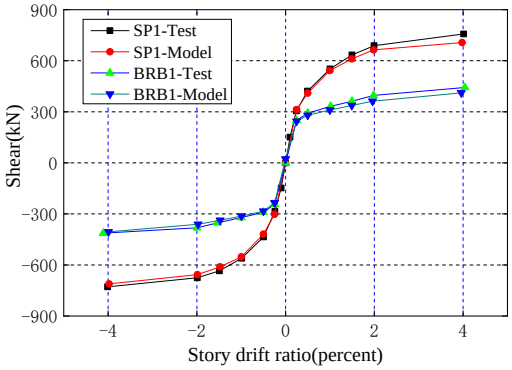

Fig. 22 Shear force-deflection curve for specimen SP1

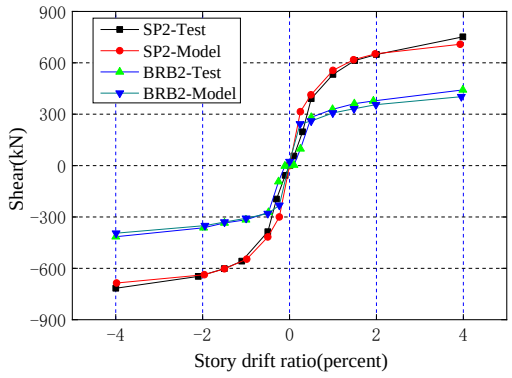

Fig. 23 Shear force-deflection curve for specimen SP2

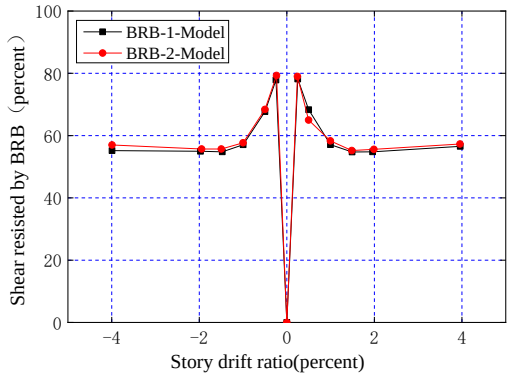

Fig. 24 Percentage of Shear Force Carried by BRB (FE Simulation).

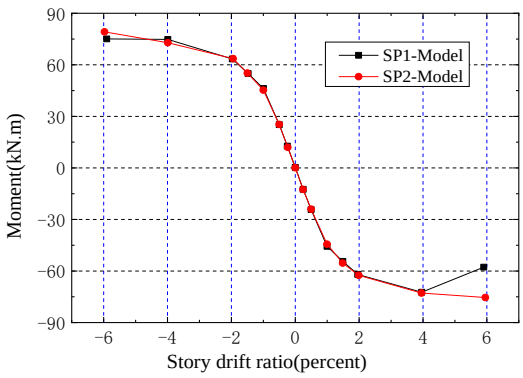

Fig. 25 Moment-rotation relationship of left beam end at 1-1 section.

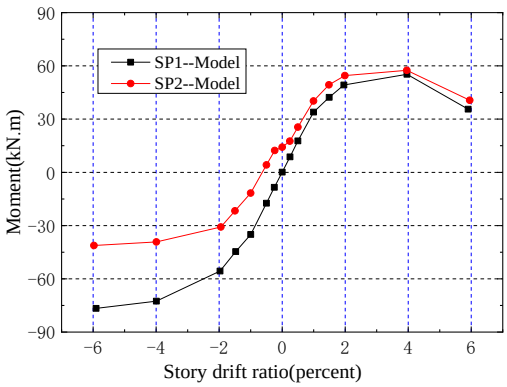

Fig. 26 Moment-rotation curves of left column end A-A section

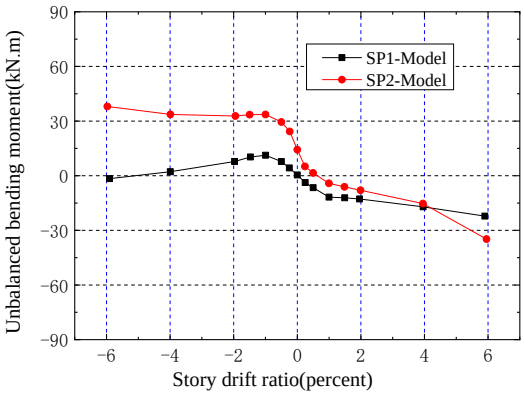

Fig. 27 Unbalanced bending moment and rotation curves at the beam-end and column-end

5.5. Analysis of forces on the beam and column ends of the frame

The relationship between the bending moment at the left beam end of the specimen and the turning angle can be observed in Fig. 25. It is evident that, with story drift angles ranging from 0 to 4% rad, both the BRB welded frame model SP1-Model and BRB hinged frame model SP2-Model exhibit yielding at the same location of the left beam-end, with very similar beam-end moments at that specific location.

The relationship between the left column-end moment and rotation at section A-A can be seen in Fig. 26. When loaded to the right, the column-end moments of the BRB welded frame model SP1-Model and BRB hinged frame model SP2-Model are moderately close. However, when loaded to the left, the column-end moment of SP1-Model is twice that of SP2-Model.

The unbalanced moments at the beam end and column end can be observed in Fig. 27 as a function of the angle of rotation. It can be seen that when loaded to the right, the unbalanced moments of both SP1-Model and SP2-Model are relatively close. However, when loaded to the left, the unbalanced moment of SP2-Model is greater, accounting for approximately 50% of the beam-end moment. This portion of unbalanced moment is generated due to the axial force of the BRB not passing through the intersection of the beam-column axis during loading. In contrast, the unbalanced moment of SP1-Model is smaller.

From the above moment diagrams, it can be seen that, throughout the entire loading process, the beam-end moment and column-end moment of SP1-Model remain relatively similar, and the unbalanced moment is small. The use of a welded connection between the BRB and the frame does not increase the beam-end moment or amplify the limit moment of the joint.

5.6. Sectional stress analysis of beam and column ends

Section 1-1, located at the plastic hinge at the left beam-end of specimens SP1-Model and SP2-Model, and section A-A at the plastic hinge at the left column-end, as shown in Fig. 2, have been selected for stress analysis. Figs. 28-30 respectively show the Mises stress distribution in these sections. Since the stress magnitude and distribution in these beam and column sections are almost unaffected by leftward and rightward loading, only the stress distribution for rightward loading is presented. From Fig. 28, it can be observed that when the story drift is less than 1.5%, the stress magnitude at section 1-1 for both SP1-Model and SP2-Model is smaller than the material yield stress of 345 MPa. The stress amplitude at this section is comparable for both specimens across different load levels. Furthermore, Figs. 29 and 30 indicate that for story drift below 1.0%, the stress magnitude at column section A-A for both SP1-Model and SP2-Model is smaller than the material yield stress of 345 MPa. The stress distribution patterns and stress amplitude magnitudes at this section are also quite similar for both specimens across different load levels. It can be seen that the welded and pin connection between the BRB and the frame have a minor impact on the stress distribution patterns and stress amplitude magnitudes at the beam-end and column-end joints.

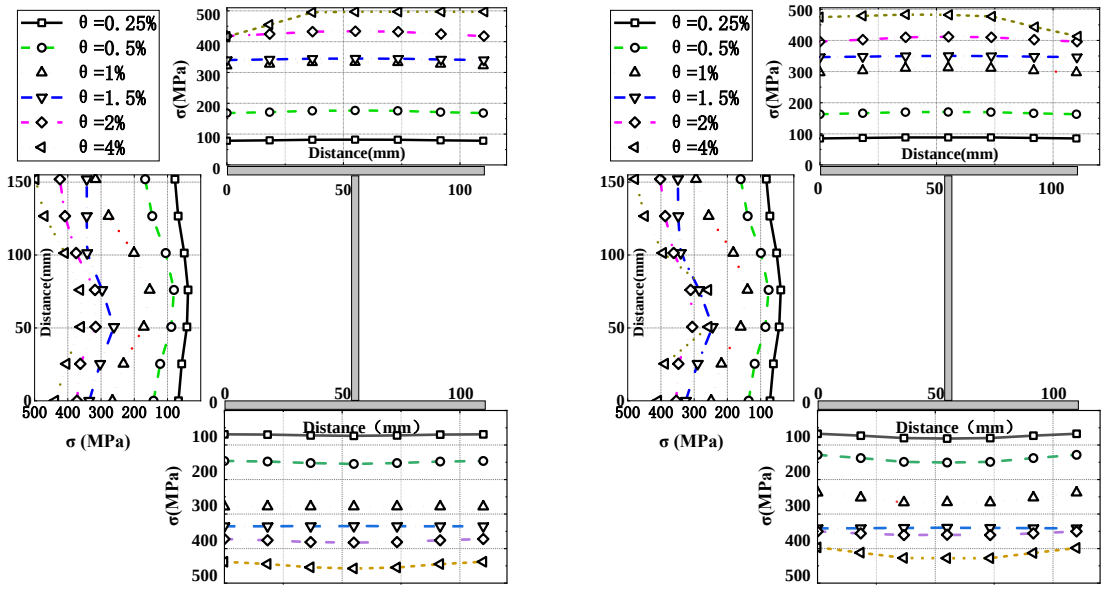

(a) Specimen SP1-Model (b) Specimen SP2-Model

Fig. 28 Mises stress distribution at steel beam section 1-1 under rightward loading for specimen

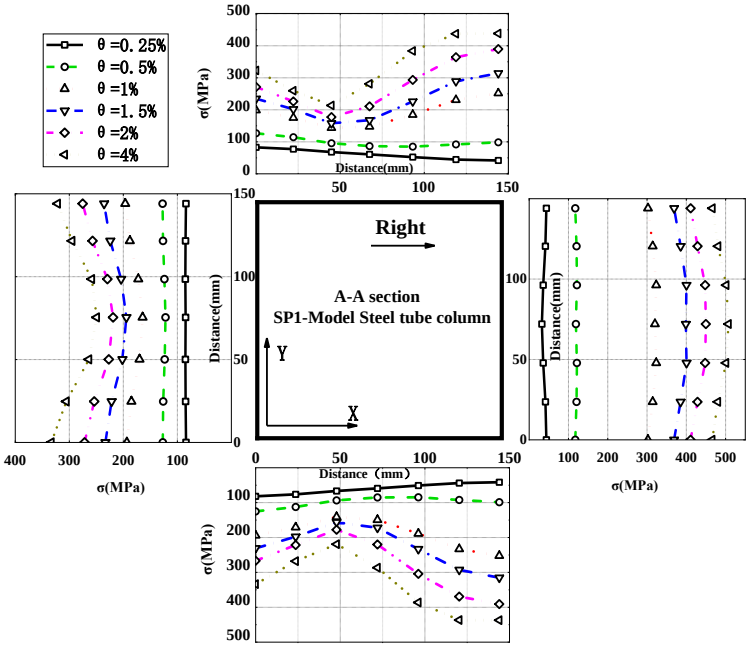

Fig. 29 Mises stress distribution at column section A-A for specimen SP1-Model under rightward loading

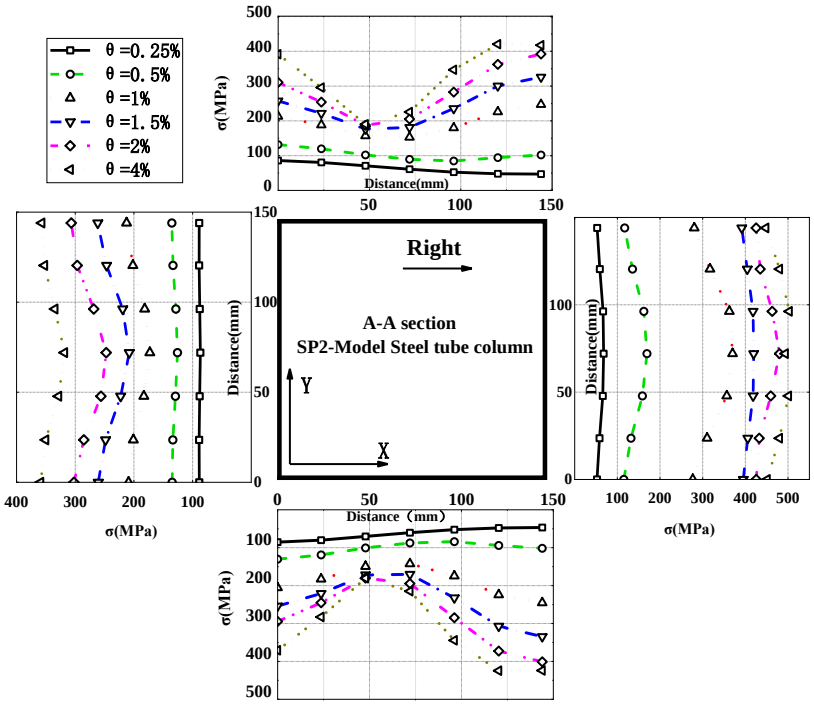

Fig. 30 Mises stress distribution at column section A-A for specimen SP2-Model under rightward loading

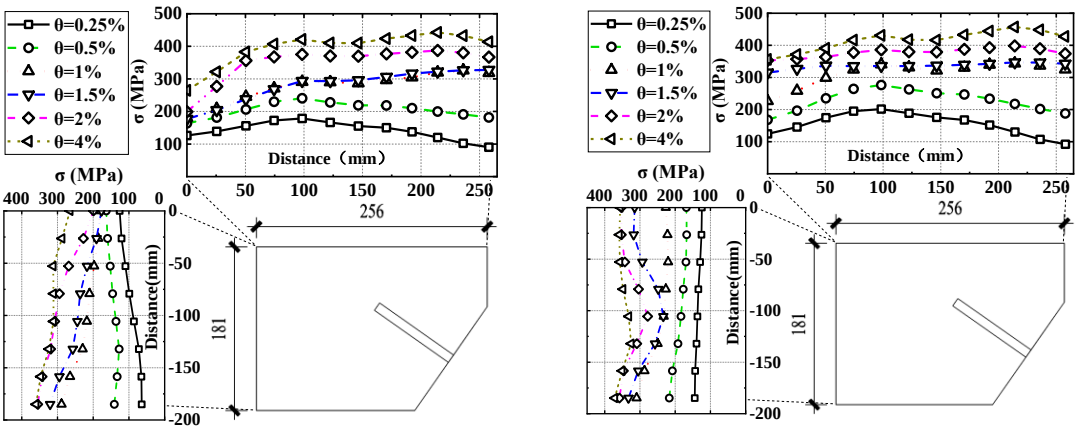

(a) Loading to the right (b) Loading to the left

Fig. 31 Mises stress distribution at the left joint weld of specimen SP1-Model

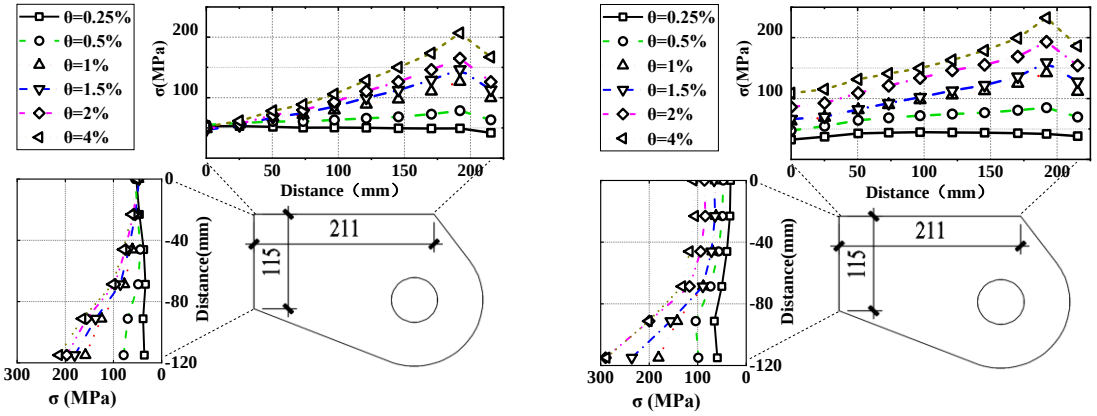

(a) Loading to the right (b) Loading to the left

Fig. 32 Mises stress distribution at the left joint weld of specimen SP2-Model

5.7. Analysis of weld stress at joints

In specimens SP1-Test and SP2-Test, the gusset plates were welded to the beams and columns using full penetration welds. On the other hand, in the finite element model, the gusset plates are 'merged' ideally to the beams and columns. The welds at the gusset plates are susceptible to failure due to concentrated forces. To understand the stress condition at the welds, the Mises stress at the joint welds at the maximum displacement angle of the first cycle during cyclic loading is selected, as shown in Figs. 31 and 32. When the story drift is less than 1.5%, the tensile and compressive stresses in the horizontal and vertical welds of the left joint of SP1-Model are all less than the yield stress of 345 MPa. Once the story drift reaches 2%, the maximum tensile and compressive stresses in the horizontal and vertical welds are both less than 400 MPa. Although the loading direction changes, the stress magnitude does not change significantly.

The stress at the left joint welds of SP2-Model is shown in Fig. 32. When the story drift angle is less than 4%, both the tensile and compressive stresses in the horizontal and vertical welds are less than 250 MPa, which is lower than the steel yield stress of 345 MPa. Similarly, the stress magnitude does not change significantly with the loading direction.

Upon comparing Figs. 31 and 32, it can be observed that the weld stress in the pin connection is significantly lower than that in the welded connection. This is because the gusset plate used in the pin connection has a thickness of 40 mm, while the gusset plate used in the welded connection has a thickness of 10 mm. At the weld location, the steel cross-sectional area at the pin connection gusset plate is approximately twice that of the welded connection gusset plate. The difference in stress is not due to the type of connection used but rather the cross-sectional area of the gusset plates.

6. Conclusion

This paper employed experimental and finite element simulation methods to compare and analyze the mechanical performance of frames featuring HSCFSSTC with buckling-restrained braces (BRBs) using both welded and pin connections under cyclic loading. Based on the analysis, the following conclusions were reached:

(1) The hysteresis loops of the BRBFs with welded and pin connections were relatively full, which satisfied the code[22] requirements for story drift limits.

(2) During the experimental failure, the plastic hinge appeared in the following order: beam ends, column base, and column ends, indicating a reasonable design. Moreover, the use of welded or pin connections in BRBFs did not significantly affect the failure mechanism of the BRBFs, the formation of plastic hinges, the energy dissipation capacity of the BRBs, the load-bearing ratio of the BRBs, or the seismic performance of the BRBFs.

(3) The result of ABAQUS analysis shows that the stress distribution patterns and magnitude at the welds of the gusset plates connecting the BRBs to frames' beams and columns, as well as the beam ends and column ends, were quite similar for both connection types. The experimental results and ABAQUS analysis results show that the BRBFs with welded and pin connections exhibit good seismic resistance and energy dissipation capabilities.

(4) When using pin connections in the BRBFs, it is important to increase the manufacturing accuracy, reduce dimensional deviations, and minimize the clearances between the pin and the connection gusset plates and connecting plates of BRBs. This helps to minimize installation errors and improve the performance of the BRBs, which ensures the seismic performance of the frames. On the other hand, welded connections overcome the drawbacks of pin connections, exhibit better performance of the BRBs, and are considered safer and more reliable. As such, welded connections have great potential for widespread application.

Acknowledgments

The authors gratefully acknowledge the financial support provided by the Key Projects of National Natural Science Foundation of China, China (51938009), the Educational Department of Liaoning Province, China (LJKMZ20220929) , the Department of Science & Technology of Liaoning province, China(2023JH6/100100053) and Shanghai Lanke Building Damping Technology Co., Ltd..

References

[1] Li Guochang, Chen Bowen, Yang Zhijian, et al. Experimental and numerical behavior of eccentrically loaded square concrete-filled steel tubular long colmns made of high-strength steel and concrete[J]. Thin-Walled Structures, 2021, 159(2):107289
[2] Li Guochang, Chen Bowen, Yang Zhijian, et al. Axial behavior of high-strength concrete-filled high strength square steel tubular stub columns. [J] Advanced Steel Construction, 2021, 17(2):158–168
[3] Saad Younas1, Ehab Hamed, Dongxu Li, Brian Uy. Eccentrically loaded concrete-filled steel tubes made with high strength materials. [J] Engineering Structures, 2023, 275
[4] Saad Younas, Ehab Hamed, et al. Effect of creep on the strength of high strength concrete-filled steel tubes. Journal of Constructional Steel Research 2023, 201
[5] Uang CM, Nakashima M, Tsai KC. Research and application of buckling-restrained braced frames[J]. Steel Structures 2004; 4(4):301–313.
[6] Atsushi Watanabe. Design and Applications of Buckling-Restrained Braces. International Journal of High-Rise Buildings. September 2018, Vol 7, No 3, 215-221.https://doi.org/10.21022/IJHRB.
2018.7.3.215
[7] Yun Zhou, Hetian Shao, Yongsheng Cao, Eric M. Lui. Application of buckling-restrained braces to earthquake-resistant design of buildings: A review. Engineering Structures 246 (2021) 112991
[8] Wang Bo,Wang Jingfeng, et al. Experimental study on seismic behavior of assembly CFST composite frames with bucking restrained braces. China Civil Engineering Journal, 2018, Vol. 51 No. 6 (in Chinese)
[9] Wigle Victoria R., Fahnestock Larry A. Buckling-restrained braced frame connection performance[J]. Journal of Constructional Steel Research, 2010，66(1)： 65-74.
[10] Keh-Chyuan Tsai, Po-Chien Hsiao.Pseudo-Dynamic Tests of a Full-Scale CFT/BRB Frame—Part I Specimen design, experiment and analysis[J]. Earthquake Engineering and Structural Dynamics 2008; 37: 1081-1098
[11] Keh-Chyuan Tsai, Po-Chien Hsiao. Pseudo-Dynamic Tests of a Full-Scale CFT/BRB Frame—Part II Seismic performance of buckling-restrained braces and connections[J]. Earthquake Engineering and Structural Dynamics 2008; 37: 1099-1115
[12] Wang Jingfeng, Gao Xiang, Li Beibei, et al. Seismic performance tests and analysis of connections between buckling restrained braces and steel frame. China Civil Engineering Journal, 2019，Vol. 52 No. 8 (in Chinese)
[13] Beibei Li, Jingfeng Wang, Yuanqing Wang. Subassemblage test and gusset rotation response of buckling-restrained braced steel frames. Structures 33 (2021) 3417–3432
[14] Mingming Jia, Kai Liu, et al. Experimental research of seismic performance of buckling-restrained braced frame with ductile connections[J]. Structures 41 (2022) 908–924
[15] Keith D. Palmer, Charles W. Roeder, et al. Experimental Performance of Steel Braced Frames Subjected to Bidirectional Loading[J]. Journal of Structural Engineering. 2013.139：1274-1284.
[16] Junda E., Leelataviwat S., Doung P. Cyclic testing and performance evaluation of buckling-restrained kneebraced frames. Journal of Constructional Steel Research 148 (2018) 154–164
[17] Wang Jingfeng ,Wang Xinle, et al. Experimental studies on seismic performance of prefabricated concrete frame structures with buckling-restrained braces. China Civil Engineering Journal,2018, Vol. 51 No. 12 (in Chinese)

[18] Jingfeng Wang, Fei Lu, Beibei Li. Subassemblage tests and analysis of buckling-restrained braced reinforced concrete frames with various gusset connections. Structures 39 (2022) 39–56
[19] Keh-Chyuan Tsai, et al, Welded end-slot connection and debonding layers for buckling-restrained braces[J]. Earthquake Engng Struct. Dyn. (2014) DOI: 10.1002/eqe
[20] Wang Cuihong. Study on Seismic Resistance and Seismic Demand Performance of BRBF Structure with Rigid Joint and Bolt Joint. Guilin university of technology.2020 (in Chinese)
[21] Sheng Pei. Experimental study on seismic performance of ultrahigh strength steel frames with buckling restrained braces[J]. Archives of Civil and Mechanical Engineering (2021) 21:164
[22] Ministry of Housing and Urban-Rural Development of the People's Republic of China, General Administration of Quality Supervision, Inspection and Quarantine of the People's Republic of China. Code for seismic design of buildings: GB 50011—2010[S]. Beijing: China Architecture & Building Press, 2010. (in Chinese)
[23] Ministry of Housing and Urban-Rural Development of the People's Republic of China. Technical specification for seismic energy dissipation of buildings: JGJ 297—2013[S]., 2013. (in Chinese)
[24] FEMA-350. Recommended Seismic Design Criteria for New Steel
[25] AISC. (2010). "Seismic provisions of structural steel building." ANSI/AISC 341-10, Chicago.
[26] Lin PC, Tsai KC, Roeder CW. Seismic design and hybrid tests of a full-scale three-story buckling-restrained braced frame using welded end connections and thin profile[J]. Earthquake Engineering and Structural Dynamics 2012; 41(5):1001–1020.
[27] Metallic materials- Tensile testing—Part 1: Method of test at room temperature. (in Chinese)
[28] Wang Wenda, Han Linhai. Nonlinear finite element analysis on mechanical performance of concrete-filled steel tubular frame structure[J]. Journal of Building Structures.2008, 29(6):75-83. (in Chinese)
[29] Shi Yongjiu, Wang Jiaojiao et al. Mechanical performance of low-yield-point steel LYP225 under cyclic loading. Journal of Southeast University (Natural Science Edition). 2014, Vol.44(6):1260-1265. (in Chinese)
[30] Chung-Che Chou, Jia-Hau Liu. Frame and Brace Action Forces on Steel Corner Gusset Plate Connections in Buckling-Restrained Braced Frames [J]. Earthquake Spectra, Volume 28, No. 2, pages 531–551, May 2012
[31] Yu YJ, Tsai KC, Li CH, Weng YT, Tsai CY. Earthquake response analyses of a full-scale five-story steel frame equipped with two types of dampers. Earthquake Engineering and Structural Dynamics 2013; 42(9):1301–1320.
[32] Li Jiaqi ,Li Guochang. Study of effect of axial compression ratio and steel core cross-section area on aseismic behaviour of buckling restrained brace-concrete frame [J].Industrial Construction 2017, 47(3)
[33] Li Guochang, Yan Hailong, Chen Bowen. Finite Element Analysis on Mechanical Behavior of the High Strength Concrete-Filled High Strength Square Steel Tube Stub Column Under Axial Compressive Loading. Journal of Shenyang Jianzhu University (Natural Science).2015, Vol.31(5):847-855 (in Chinese)